IEEE Access
Multidisciplinary | Rapid Review | Open Access Journal

Received 15 January 2024, accepted 7 February 2024, date of publication 9 February 2024, date of current version 16 February 2024.

Digital Object Identifier 10.1109/ACCESS.2024.3365053

RESEARCH ARTICLE

AC-Side Impedance-Based Stability Assessment in Grid-Forming Modular Multilevel Converters

MEHRDAD NAHALPARVARI, (Graduate Student Member, IEEE), MOHSEN ASOODAR, (Graduate Student Member, IEEE), STAFFAN NORRGA, (Member, IEEE), AND HANS-PETER NEE, (Fellow, IEEE)
School of Electrical Engineering and Computer Science, KTH Royal Institute of Technology, 100 44 Stockholm, Sweden

Corresponding author: Mehrdad Nahalparvari (mnah@kth.se)

This work was supported in part by Energimyndigheten (the Swedish Energy Agency), in part by Svenska kraftnät (SvK), and in part by Réseau de Transport d'Électricité (RTE) France.

ABSTRACT Grid-forming converters can emulate the behavior of a synchronous generator through frequency droop control. The stability of grid-forming modular multilevel converters can be studied via the impedance-based stability criterion. This paper presents an ac-side impedance model of a grid-forming modular multilevel converter which includes a complete grid-forming control structure. The impact of different control schemes and parameters on the closed-loop output impedance of the converter is thoroughly analyzed and the learnings have been used in mitigating undesired control interactions with the grid. The results are verified through simulations in time- and frequency-domains along with experiments on a down-scaled laboratory prototype.

INDEX TERMS Control interaction, frequency-domain analysis, grid-forming control, harmonic linearization, impedance modeling, modular multilevel converter (MMC), stability.

I. INTRODUCTION

Voltage source converter (VSC)-based high voltage direct current (HVDC) transmission systems enable large-scale integration of renewable energy sources and efficient transfer of bulk power over long distances [1], [2]. The modular multilevel converter (MMC) is the preferred topology in HVDC transmission systems due to its modularity, scalability, and low distortions [3].

VSCs are conventionally controlled as current sources and in a grid-following manner where the synchronization is realized by a phase-locked loop (PLL). This makes them prone to stability issues, especially in weak grid conditions due to the inadequacy of PLLs in tracking disturbed voltage angles [4]. Considering a shift toward a cleaner energy matrix, the grid stiffness may substantially decrease in the future as synchronous generators are replaced by inverter-based resources. Grid-forming control schemes primarily control the ac-side voltage and operate the converter as a voltage source. By using a power-frequency droop function, they also emulate the behavior of a synchronous generator and add virtual inertia to the power system, essentially enabling operation in weak grid conditions [5], [6].

VSC-based HVDC transmission systems are prone to system instabilities that need to be predicted, analyzed, and mitigated [7], [8], [9], [10]. The stability of power electronics-based systems, including VSC-HVDC systems, can be evaluated using several methods such as passivity-based analysis, eigenvalue-based analysis, the net-damping criterion, and the impedance-based stability criterion [11]. In the latter, the grid-connected converter system can be partitioned into a source and load subsystem where the converter is modeled as an impedance behind a voltage source (Thévenin equivalent) or an admittance in parallel to a current source (Norton equivalent). The small-signal stability of the system is then assessed via the ratio of the source and load impedance, known as the minor-loop gain. Accurate stability assessment requires either precise measurement of the converter's impedance at its terminals or a well-constructed model of the same. Nonetheless, owing

The associate editor coordinating the review of this manuscript and approving it for publication was Xueguang Zhang.

to the nonlinearities introduced by the converter dynamics, impedance modeling of MMCs is challenging and intricate.

Research on impedance modeling of grid-following VSC-based HVDC systems and MMCs is abundant [12], [13], [14], [15], [16], [17], [18], [19], [20]. Several new studies analyze converter-driven stability with regards to grid-forming converters. For instance, stability assessment of grid-forming control applied to a two-level VSC is studied in [21]. An ac-side impedance model in the $\alpha\beta$-domain is developed, based on which a subsynchronous control interaction with a strong grid is identified. The study includes experimental time-domain verification of the control interaction. However, it lacks experimental frequency-domain verification of the developed impedance model. Later in [22], the authors complement the prior study by a control decomposition methodology based on tuning of the controllers to improve the stability margin. It has been shown both in [21] and [23] that the root cause of impedance interaction and instability is the non-passivity of the converter around the fundamental frequency introduced by the resonant/integral action of the voltage control loop.

A few studies have also analyzed the impact of grid-forming control on the closed-loop output impedance of MMCs. For instance, Reference [24] has presented an ac-side impedance model of a voltage-controlled MMC regulated via single-loop and dual-loop structures. Nevertheless, the power droop functions emulating a synchronous machine have been neglected. Moreover, the regulators have been limited to proportional-resonant types used in the *abc* or $\alpha\beta$ stationary reference frame. Reference [25] has analyzed the stability of a voltage-controlled MMC connected to a wind farm. The droop functions and dual-loop voltage control are however not included. The authors of [26] have analyzed the ac- and dc-side impedances of an MMC with grid-forming control. In this study, the inner-loop voltage and current control loops have been ignored and the analysis has been limited to outer-loop droop functions. Harmonic instabilities have been identified and virtual impedances have been proposed to damp the unstable oscillations. Reference [27] has conducted an impedance based small-signal stability analysis for MMCs with power synchronization control and proposed a virtual impedance loop on the computed insertion indices that handles the negative resistance below the fundamental frequency. In [25], [26], and [27], the cause of instability has also been determined as the non-passivity of the converter in sub-synchronous frequencies, similar to that present in generic two-level converters. High frequency unstable oscillations may also happen in grid-forming MMCs connected to wind farms [28]. As described above, the investigation into the influence of grid-forming control on the small-signal stability of VSCs represents an ongoing area of research. None of the studies introduced above, however, have included an experimental verification of the developed impedance models, time-domain verification of instability scenarios, and the workings of their proposed stabilizing loops.

This paper presents an accurate impedance model of a grid-forming MMC which takes into account the entire grid-forming control structure not excluding the inner voltage and current control loops, or the outer droop functions. The effect of using both single-loop voltage control and dual-loop voltage control on the ac-side impedance of the converter has been investigated and the small-signal stability of the system is analyzed. It has been shown that instabilities can occur under certain control and system parameters due to the interaction of the grid impedance and the negative resistance behavior of the converter's output impedance that is introduced by the voltage control loop. The instability and the frequency of the unstable oscillations can be predicted by impedance analysis.

Compared to the state-of-the-art in the literature, the contributions of this work are the proposal of three novel instability mitigation strategies based on 1) cross-coupled virtual resistance on ac-side currents, 2) low-pass filters on the ac-side currents, and 3) lead compensators on the PCC voltage that improve the stability margin of the system. Moreover, not only the developed frequency-domain impedance models are verified on a down-scaled laboratory prototype, but also the prediction of the instability and the efficacy of the mitigation strategies have been verified on power electronics hardware.

The paper is organized as follows: Section II describes the converter dynamics and discusses the considered control solutions for grid-forming MMCs. Section III describes the derivation procedure of the ac-side impedance for all control solutions. Section IV presents and discusses the results of the study, analyzes the effect of different control schemes and parameters on converter's impedance, assesses small-signal system stability, and proposes methods to improve stability margin. Finally, Section V draws conclusions based on the results.

II. SYSTEM MODEL

The MMC for ac/dc conversion comprises three phase-legs with two arms within each leg. The converter arms consist of a number of cascaded submodules (SMs) and an arm inductor designed to reduce the harmonic distortion in arm currents and prevent high transient currents. Fig. 1 shows the single-line diagram of a grid-connected MMC in which L and L_g denote the arm and grid inductances, respectively, and R and R_g denote the arm and grid resistances, respectively. A phase-domain impedance model is derived based on dynamics of the converter and the considered control scheme. For the sake of brevity, throughout the text, a per-phase modeling approach is taken where the subscript indicating specific phases is dropped.

A. CONVERTER DYNAMICS

A dynamic model of the MMC is adopted in which the switching operations are neglected and balanced submodule capacitor voltages are assumed within an arm [29]. The

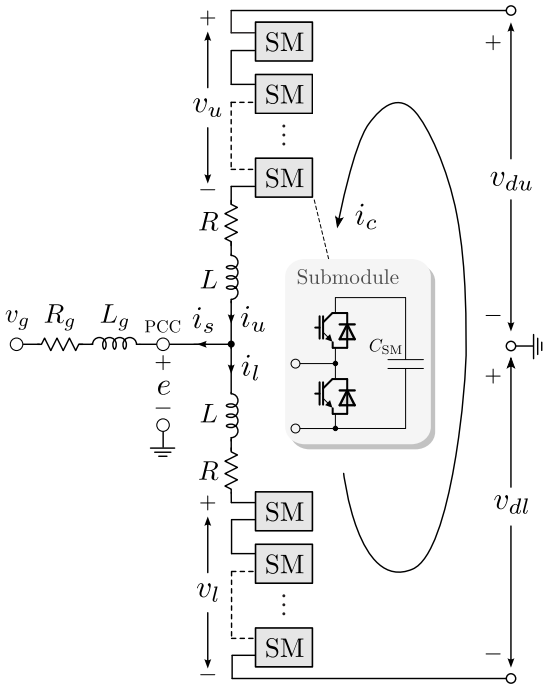

FIGURE 1. Single-line diagram of a modular multilevel converter (MMC). A half-bridge submodule configuration is shown as an example.

dynamics governing the MMC can then be obtained as

$$\begin{cases} L\dfrac{\mathrm{d}i_u}{\mathrm{d}t} = -Ri_u + v_{du} - v_u - e\,, & (1)\\ L\dfrac{\mathrm{d}i_l}{\mathrm{d}t} = -Ri_l + v_{dl} - v_l + e\,, & (2)\\ v_{u,l} = n_{u,l}v^{\Sigma}_{Cu,l}\,, & (3)\\ v^{\Sigma}_{Cu,l} = \dfrac{N}{C_{\mathrm{SM}}}\displaystyle\int n_{u,l}i_{u,l}\,\mathrm{d}t + v^{\Sigma}_{C0}\,, & (4)\end{cases}$$

where i_u (i_l) is the upper (lower) arm current, v_{du} (v_{dl}) is the upper (lower) dc-side voltage, and e is the voltage of the point of common coupling (PCC). Arm voltages are denoted by $v_{u,l}$, and $v^{\Sigma}_{Cu,l}$ are the sum-capacitor voltages. C_{SM} is the submodule capacitance, N is the number of submodules and v^{Σ}_{C0} is the initial sum capacitor voltage. Moreover, the (upper and lower arm) insertion indices, indicated by $n_{u,l}$, are the outputs of the control system computed in a closed-loop fashion.

B. CONVERTER CONTROL

VSC control is often implemented in a cascaded manner, with outer control loops setting the reference for the inner loops [1]. The grid-forming control scheme for MMCs is shown in Fig. 2. In grid-forming control, the primary control objectives are controlling the converter output voltage while transferring active and reactive power. The powers are controlled via droop functions which set the reference for the faster inner-loop voltage control. Voltage control can be realized either with a single-loop, or can also nest a current control loop whose primary objective is to control transient currents, referred to commonly in the literature as dual-loop control [23]. The outputs of the control system is then modulated (by e.g., phase-shifted carrier pulse-width modulation) to generate the switching commands which are applied to the submodules of the converter. In addition, a circulating current control loop, suppresses the second-order harmonic currents that appear in the arm currents.

Assuming $v_{du} = v_{dl} = v_{\mathrm{dc}}/2$, adding and subtracting upper/lower arm current equations yields

$$\frac{L}{2}\frac{\mathrm{d}i_s}{\mathrm{d}t} + \frac{R}{2}i_s = v_s - e \qquad \text{with } v_s = \frac{-v_u + v_l}{2} \tag{5a}$$

$$L\frac{\mathrm{d}i_c}{\mathrm{d}t} + Ri_c = \frac{v_{\mathrm{dc}}}{2} - v_c \qquad \text{with } v_c = \frac{v_u + v_l}{2}\,, \tag{5b}$$

where v_s is the voltage driving the ac-side current i_s and v_c is the voltage driving the circulating current i_c.

The reference voltages $v_s^\star$ and $v_c^\star$ can be used to compute the insertion indices of the arms. Assuming a direct voltage control scheme (also known as direct modulation), we define

$$n_u = \frac{v_c^\star - v_s^\star}{v_{\mathrm{dc}}} \quad \text{and} \quad n_l = \frac{v_c^\star + v_s^\star}{v_{\mathrm{dc}}}\,, \tag{6}$$

which provides an asymptotically stable system [30].

Ideal insertion indices can also be considered where the arm reference voltages are normalized by the measured sum capacitor voltages. Referred to as closed-loop voltage control (or compensated modulation), the insertion indices in this case can then be calculated by

$$n_u = \frac{v_c^\star - v_s^\star}{v^{\Sigma}_{Cu}} \quad \text{and} \quad n_l = \frac{v_c^\star + v_s^\star}{v^{\Sigma}_{Cl}}\,. \tag{7}$$

With closed-loop voltage control, the internal dynamics of the MMC are only marginally stable and arm-balancing control is required to stabilize the system [31]. In this work, a direct voltage control scheme is considered. This choice is motivated by the fact that the studied stability problem is related to the non-passivity of the converter introduced by the control structure shown in Fig. 2, which is present irrespective of the choice of the modulation scheme.

In a three-phase system, the powers are calculated in the dq-frame as

$$P = \frac{3}{2}(e_d i_{sd} + e_q i_{sq}) \tag{8}$$

$$Q = \frac{3}{2}(e_q i_{sd} - e_d i_{sq})\,, \tag{9}$$

where e_{dq} is the PCC voltage in the synchronous (dq) reference frame and $i_{s,dq}$ is the output current in the dq-frame.

III. AC-SIDE IMPEDANCE CALCULATION

To calculate the ac-side impedance, a fixed-frequency perturbation is superimposed on the terminal voltage or current. Then, the response of converter and control variables is calculated for the applied perturbation under frequency sweeps of the perturbation source [32].

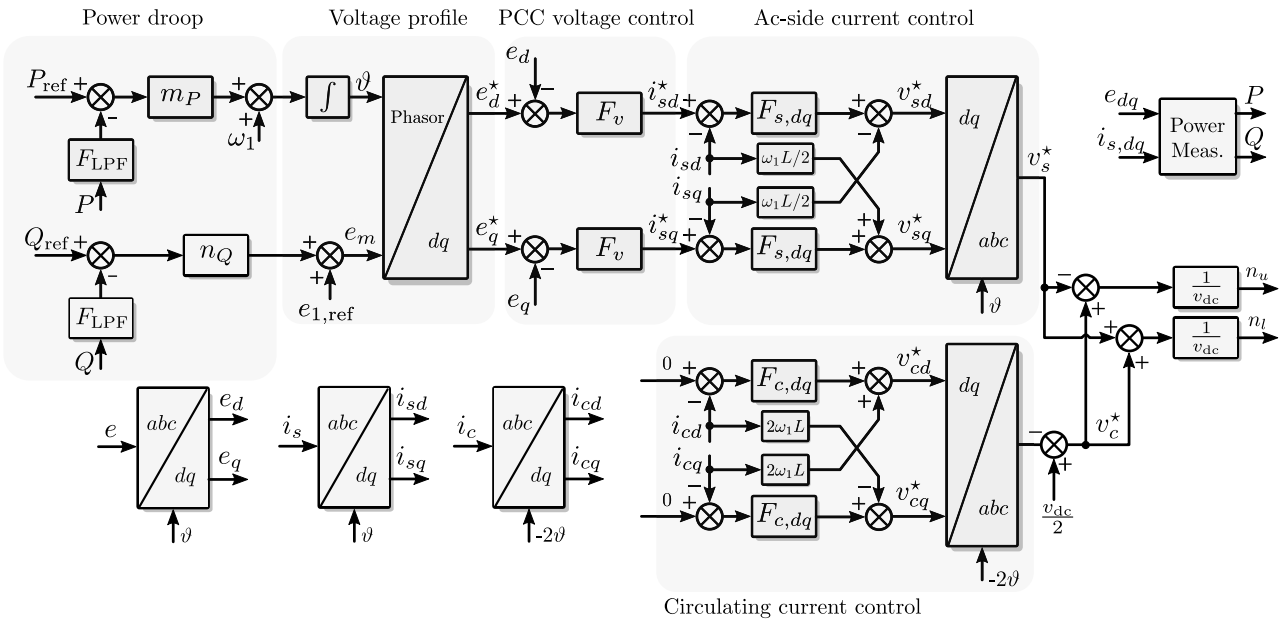

FIGURE 2. Droop-controlled dual-loop grid-forming control structure for an MMC.

In this work, a three-phase balanced small-signal perturbation voltage is superimposed on the grid voltage, i.e.,

$$\begin{cases} v_{ga} = v_{g,1}\cos(\omega_1 t + \phi_1) + v_p \cos(\omega_p t + \phi_p) \\ v_{gb} = v_{g,1}\cos(\omega_1 t - \dfrac{2\pi}{3} + \phi_1) + v_p \cos(\omega_p t - \dfrac{2\pi}{3} + \phi_p) \\ v_{gc} = v_{g,1}\cos(\omega_1 t + \dfrac{2\pi}{3} + \phi_1) + v_p \cos(\omega_p t + \dfrac{2\pi}{3} + \phi_p)\,, \end{cases} \tag{10}$$

such that $|V_g(j\omega_p)| \ll |V_g(j\omega_1)|$, i.e., the perturbation is small-signal. In (10), V_g denotes the Fourier coefficient of v_g, ω_p is the angular perturbation frequency, ω_1 is the fundamental frequency, and ϕ_1 is the initial phase angle of the grid voltage. ϕ_p is the initial angle of the perturbation signal.

The harmonic responses of the converter and the control variables to the perturbation are calculated in the frequency-domain. Multiplication of the converter variables in the time-domain in (3)–(4) leads to a convolution of their spectra in the frequency-domain [18]. The most significant of these harmonic responses appear at a combination of the perturbation frequency f_p and integer multiples of the fundamental frequency f_1, i.e., $f = \{f_p \pm nf_1\}$, $n \in \mathbb{Z}$. To keep the complexity of the resulting impedance model at bay, $n \leq 3$ is assumed in this work.

In the following, the harmonic responses of the converter and control variables to the applied perturbation are evaluated and calculated. The capitalized letters indicate the Fourier coefficient of the variables. Due to the symmetry of the three-phase topology, frequency-domain analysis of a single-arm—in this case upper-arm of phase a—suffices.

A. RESPONSE OF THE CONVERTER VARIABLES

The harmonic responses of the converter variables, i_u, v_u, and v_{Cu}^{Σ}, to the applied perturbation are calculated at $j\omega_p$. The rest of the expressions for other frequencies (including the steady-state frequencies) are derived in a similar fashion and are given in [19].

1) ARM AND SUM-CAPACITOR VOLTAGES

The multiplication in the time-domain in (3) and (4) translates to the convolution of the elements in the frequency-domain. From (3), the perturbation frequency component of the arm voltage at $j\omega_p$ can be derived as

$$\begin{aligned} &V_u(j\omega_p) \\ &= V_{Cu}^{\Sigma}(j\omega_p)N_u(0) + N_u(j\omega_p)V_{Cu}^{\Sigma}(0) \\ &\quad + V_{Cu}^{\Sigma}(j\omega_p - j\omega_1)N_u(j\omega_1) + N_u(j\omega_p - j\omega_1)V_{Cu}^{\Sigma}(j\omega_1) \\ &\quad + V_{Cu}^{\Sigma}(j\omega_p + j\omega_1)\overline{N_u(j\omega_1)} + N_u(j\omega_p + j\omega_1)\overline{V_{Cu}^{\Sigma}(j\omega_1)} \\ &\quad + N_u(j\omega_p - j2\omega_1)V_{Cu}^{\Sigma}(j2\omega_1) + N_u(j\omega_p + j2\omega_1)\overline{V_{Cu}^{\Sigma}(j2\omega_1)}\,. \end{aligned} \tag{11}$$

In a similar fashion, the perturbation frequency component of V_{Cu}^{Σ} at $j\omega_p$ is calculated using (4) as

$$\begin{aligned} &V_{Cu}^{\Sigma}(j\omega_p) \\ &= \frac{1}{j\omega_p C}\big[I_u(j\omega_p)N_u(0) + N_u(j\omega_p)I_u(0) \\ &\quad + I_u(j\omega_p - j\omega_1)N_u(j\omega_1) + N_u(j\omega_p - j\omega_1)I_u(j\omega_1) \\ &\quad + I_u(j\omega_p + j\omega_1)\overline{N_u(j\omega_1)} + N_u(j\omega_p + j\omega_1)\overline{I_u(j\omega_1)}\big]\,. \end{aligned} \tag{12}$$

The rest of the perturbation frequency components and the steady-state solution are given in [19]. The bar denotes the complex conjugate operation.

2) ARM CURRENTS

The response of i_u to the applied perturbation can be calculated from (1) as

$$I_u(j\omega) = \frac{-V_u(j\omega) - E(j\omega)}{j\omega L + R}, \tag{13}$$

where $\omega \in \{\omega_p \pm n\omega_1\},\ n \in \mathbb{N}, n \leq 3$.

3) AC-SIDE VECTOR-CURRENTS

The dq-components of the ac-side current can be obtained by Park transformation as

$$i_{sd} = i_{s\alpha}a + i_{s\beta}b \qquad i_{sq} = i_{s\beta}a - i_{s\alpha}b\,, \tag{14}$$

where

$$a = \cos(\vartheta) \quad \text{and} \quad b = \sin(\vartheta)\,, \tag{15}$$

and $i_{s\alpha}$ and $i_{s\beta}$ are the ac-side currents in the $\alpha\beta$-reference frame, and ϑ is obtained from the active power droop characteristics.

After mathematical manipulation, the responses of the ac-side current in the dq-frame to the applied perturbation can be obtained as

$$\begin{bmatrix} I_{sd}(j\omega_p - j\omega_1) \\ I_{sq}(j\omega_p - j\omega_1) \end{bmatrix} = \begin{bmatrix} \overline{A(j\omega_1)} & -j\overline{B(j\omega_1)} \\ -\overline{B(j\omega_1)} & -j\overline{A(j\omega_1)} \end{bmatrix} I_s(j\omega_p)\,, \tag{16}$$

where $I_s(j\omega_p) = 2I_u(j\omega_p)$. The steady-state frequency components $A(j\omega_1)$ and $B(j\omega_1)$ are given in the Appendix.

4) CIRCULATING VECTOR-CURRENTS

The circulating currents have a dominant negative sequence double line frequency component. We define

$$a' = \cos(-2\vartheta) \quad \text{and} \quad b' = \sin(-2\vartheta)\,, \tag{17}$$

used in the Park transformation of the circulating currents.

The responses of the circulating currents in the synchronous reference frame to the applied ac-side perturbation are also calculated similarly as

$$\begin{aligned} I_{cd}(j\omega_p - j\omega_1) &= I_u(j\omega_p + j\omega_1)(\overline{A'(j2\omega_1)} + j\overline{B'(j2\omega_1)}) \\ &\quad + I_u(j\omega_p - 3j\omega_1)(A'(j2\omega_1) - jB'(j2\omega_1)) \end{aligned} \tag{18a}$$

$$\begin{aligned} I_{cq}(j\omega_p - j\omega_1) &= I_u(j\omega_p + j\omega_1)(-\overline{B'(j2\omega_1)} + j\overline{A'(j2\omega_1)}) \\ &\quad + I_u(j\omega_p - 3j\omega_1)(-B'(j2\omega_1) - jA'(j2\omega_1))\,. \end{aligned} \tag{18b}$$

5) PCC VOLTAGE

Via Kirchhoff's voltage law applied to the circuit in Fig. 1, the response of the PCC voltage to the applied perturbation can be calculated as

$$E(j\omega) = (R_g + j\omega L_g)I_s(j\omega) + V_g(j\omega)\,, \tag{19}$$

where $\omega \in \{\omega_p, \omega_p - 2\omega_1\}$ due to the mirror frequency effect [33], and $V_g(j\omega) = e_p/2$, with e_p as the amplitude of the perturbation.

Vector-voltage control has been applied in this work. Therefore, the dq-components of the PCC voltage can be obtained by the Park transformation as

$$e_d = e_\alpha a + e_\beta b \qquad e_q = e_\beta a - e_\alpha b\,, \tag{20}$$

where e_α and e_β are the PCC voltages in the $\alpha\beta$-reference frame.

After mathematical manipulation, the Fourier coefficients E_d and E_q can be obtained as

$$\begin{aligned} E_d(j\omega_p - j\omega_1) &= E(j\omega_p)(\overline{A(j\omega_1)} - j\overline{B(j\omega_1)}) \\ &\quad + E(j\omega_p - j2\omega_1)(A(j\omega_1) + jB(j\omega_1)) \end{aligned} \tag{21a}$$

$$\begin{aligned} E_q(j\omega_p - j\omega_1) &= -E(j\omega_p)(\overline{B(j\omega_1)} + j\overline{A(j\omega_1)}) \\ &\quad + E(j\omega_p - j2\omega_1)(-B(j\omega_1) + jA(j\omega_1))\,, \end{aligned} \tag{21b}$$

B. RESPONSE OF THE CONTROL VARIABLES

The response of the control system comprising the outer power synchronization loop, the inner ac-side current and PCC voltage loops, and the circulating current control loop is analyzed in the frequency-domain.

1) ACTIVE AND REACTIVE POWER

The active and reactive power droops set the PCC voltage amplitude and angle, respectively. Linearizing (8) and (9) around the steady-state trajectory yields

$$\begin{aligned} P(j\omega) &= \frac{3}{2}[E_d(j\omega)I_{sd}(0) + I_{sd}(j\omega)E_d(0) \\ &\quad + E_q(j\omega)I_{sq}(0) + I_{sq}(j\omega)E_q(0)]\,, \end{aligned} \tag{22}$$

$$\begin{aligned} Q(j\omega) &= \frac{3}{2}[E_q(j\omega)I_{sd}(0) + I_{sd}(j\omega)E_q(0) \\ &\quad - E_d(j\omega)I_{sq}(0) + I_{sq}(j\omega)E_d(0)]\,. \end{aligned} \tag{23}$$

where $\omega = \omega_p - \omega_1$.

2) VOLTAGE PROFILE MANAGEMENT

The harmonic response of the desired PCC voltage magnitude e_{m} can be calculated by evaluating the reactive power control loop in Fig. 2 as

$$E_{\mathrm{m}}(j\omega) = -Q(j\omega) \cdot F_{\mathrm{LPF}}(j\omega) \cdot n_Q\,, \tag{24}$$

where $\omega = \omega_p - \omega_1$, due to the Park transformation. The transfer function F_{LPF} is a first-order low-pass filter of the form

$$F_{\mathrm{LPF}}(s) = \frac{\omega_c}{s + \omega_c}\,, \tag{25}$$

and n_Q is the reactive power droop gain.

The PCC voltage reference phasor is generated by

$$e_{\mathrm{ref}} = e_{\mathrm{m}}e^{j\vartheta}\,. \tag{26}$$

Similar to the actual PCC voltage, the references have harmonic responses at $\omega = \{\omega_p, \omega_p \pm 2\omega_1\}$. The harmonic responses of this reference voltage are calculated as

$$\begin{bmatrix} E_{\text{ref}}(j\omega_p) \\ E_{\text{ref}}(j\omega_p - j2\omega_1) \end{bmatrix} = \begin{bmatrix} B(j\omega_1) \\ \overline{B(j\omega_1)} \end{bmatrix} E_{\text{m}}(j\omega_p - j\omega_1)\,. \tag{27}$$

Subsequently, the harmonic response of the PCC reference voltages in the dq-frame can be obtained as

$$E_d^\star(j\omega_p - j\omega_1) = 0 \tag{28a}$$

$$E_q^\star(j\omega_p - j\omega_1) = -2[E_{\text{ref}}(j\omega_p)\big(\overline{B(j\omega_1)} + j\overline{A(j\omega_1)}\big) + E_{\text{ref}}(j\omega_p - j2\omega_1)\big(B(j\omega_1) + jA(j\omega_1)\big)]\,. \tag{28b}$$

3) PCC VOLTAGE CONTROL

The perturbation frequency response of $i^\star_{s,dq}$ can be calculated from (28) as

$$I^\star_{s,dq}(j\omega) = F_v(j\omega)\big(E^\star_{dq}(\omega) - E_{dq}(\omega)\big)\,, \tag{29}$$

where $\omega = \omega_p - \omega_1$, and $F_v(s)$ is a proportional-integral (PI) controller given by

$$F_v(s) = k_{p,v} + \frac{k_{i,v}}{s}\,. \tag{30}$$

4) AC-SIDE VECTOR-CURRENT CONTROL

Similarly, the response to the applied perturbation can be calculated as

$$V^\star_{sd}(j\omega) = F_{s,dq}(j\omega)[I^\star_{sd}(j\omega) - I_{sd}(j\omega)] - \frac{\omega_1 L}{2} I_{sq}(j\omega) \tag{31a}$$

$$V^\star_{sq}(j\omega) = F_{s,dq}(j\omega)[I^\star_{sq}(j\omega) - I_{sq}(j\omega)] + \frac{\omega_1 L}{2} I_{sd}(j\omega)\,, \tag{31b}$$

where $\omega = \omega_p - \omega_1$, and $F_{s,dq}(s)$ is a PI controller given by

$$F_{s,dq}(s) = \alpha_s \frac{L}{2}(1 + \frac{2\alpha_1}{s})\,. \tag{32}$$

The Fourier coefficients of the converter output voltage references in the phase-domain can be obtained through dq/abc transformation as

$$V^\star_s(j\omega_p) = V^\star_{sd}(j\omega_p - \omega_1)A(j\omega_1) - V^\star_{sq}(j\omega_p - j\omega_1)B(j\omega_1) \tag{33a}$$

$$V^\star_s(j\omega_p - j2\omega_1) = V^\star_{sd}(j\omega_p - \omega_1)\overline{A(j\omega_1)} - V^\star_{sq}(j\omega_p - j\omega_1)\overline{B(j\omega_1)} \tag{33b}$$

5) CIRCULATING VECTOR-CURRENT CONTROL

The small-signal response of the voltages driving the circulating currents can be calculated as

$$V^\star_{cd}(j\omega) = -F_{c,dq}(j\omega)I_{cd}(j\omega) + 2\omega_1 L I_{cq}(j\omega) \tag{34a}$$

$$V^\star_{cq}(j\omega) = -F_{c,dq}(j\omega)I_{cq}(j\omega) - 2\omega_1 L I_{cd}(j\omega)\,, \tag{34b}$$

where $\omega = \omega_p - \omega_1$, and $F_{c,dq}(s)$ is a PI controller given by

$$F_{c,dq}(s) = \alpha_c L(1 + \frac{2\alpha_2}{s})\,. \tag{35}$$

With the dq/abc transformation, the harmonic responses of the reference voltages driving circulating currents in the phase-domain can be obtained as

$$V^\star_c(j\omega_p + j\omega_1) = V^\star_{cq}(j\omega_p - j\omega_1)B'(2j\omega_1) - V^\star_{cd}(j\omega_p - j\omega_1)A'(j2\omega_1) \tag{36a}$$

$$V^\star_c(j\omega_p - j3\omega_1) = V^\star_{cq}(j\omega_p - j\omega_1)\overline{B'(j2\omega_1)} - V^\star_{cd}(j\omega_p - j\omega_1)\overline{A'(j2\omega_1)} \tag{36b}$$

6) INSERTION INDEX CALCULATION

The small-signal perturbation of insertion indices follows (6) and thus obtained as

$$N_u(j\omega) = \frac{V^\star_c(j\omega) - V^\star_s(j\omega)}{v_{\text{dc}}}\,, \tag{37}$$

where ω is the available frequency components in the insertion indices according to the chosen control solution.

C. DERIVATION OF THE AC-SIDE IMPEDANCE

Based on the expressions describing the frequency responses of the converter and control variables to the applied perturbation, Eqs. (11)–(37), a linear system of equations with the unknown variables of the form

$$U_p \mathbf{x}_p = T_p\,, \tag{38}$$

is formulated where U_p comprises the coefficients of the linear system, T_p consists of the constant terms in the equations, and x_p contains the system variables

$$\begin{aligned}\mathbf{x}_p = \big[&I_u(j\omega_p - j3\omega_1), \cdots, I_u(j\omega_p + j3\omega_1),\\ &V_u(j\omega_p - j3\omega_1), \cdots, V_u(j\omega_p + j3\omega_1),\\ &V^\Sigma_{Cu}(j\omega_p - j3\omega_1), \cdots, V^\Sigma_{Cu}(j\omega_p + j3\omega_1),\\ &N_u(j\omega_p - j3\omega_1), \cdots, N_u(j\omega_p + j3\omega_1),\\ &E(j\omega_p), E(j\omega_p - j2\omega_1)\big]^T\,.\end{aligned} \tag{39}$$

The elements of U_p and T_p for I_u, V_u, and V^Σ_{Cu} at $f \in \{f_p \pm f_1, f_p \pm 2f_1, f_p \pm 3f_1\}$ are given in [19], while those of the rest of the variables are obtained in (16)–(37). Solving the linear system of equations (39) yields the harmonic responses of all considered converter and control variables at the considered frequencies. It is worth mentioning that the developed impedance model is valid for a specified steady-state point at which the mathematical problem is solved.

The injected perturbation frequency f_p yields harmonic responses through the grid impedance in the PCC voltage E and the converter current I_s, at f_p and $f_p - 2f_1$, respectively. The assumption of small-signal study is valid here; the responses to the applied perturbation signal must be small signal, i.e., they should not diverge the system from its steady-state point. While the impact of the cross-coupling

impedance terms are smaller than that of the direct terms, for accurate stability assessment, a multiple-input multiple-output (MIMO) stability problem needs to be analyzed. Accordingly, the ac-side impedance of the converter is a 2×2 MIMO matrix of the form

$$\mathbf{Z}_{\text{ac}} = \begin{bmatrix} Z_{11} & Z_{12} \\ Z_{21} & Z_{22} \end{bmatrix}, \tag{40}$$

which indicates that four distinct equations are needed to calculate the four unknown elements of the impedance matrix. Therefore, two independent perturbation signals need to be injected from which the responses of the PCC voltage and current need to be captured at f_p and $f_p - 2f_1$. The perturbations must be chosen to be linearly independent. Thus, firstly a positive sequence perturbation signal of the form

$$\begin{cases} v_{pa,1} = v_p \cos(\omega_p t + \phi_p) \\ v_{pb,1} = v_p \cos(\omega_p t - \dfrac{2\pi}{3} + \phi_p) \\ v_{pc,1} = v_p \cos(\omega_p t + \dfrac{2\pi}{3} + \phi_p), \end{cases} \tag{41}$$

is applied, followed by a negative sequence perturbation signal of the form

$$\begin{cases} v_{pa,2} = v_p \cos\left[(\omega_p - 2\omega_1)t + \phi_p\right] \\ v_{pb,2} = v_p \cos\left[(\omega_p - 2\omega_1)t + \dfrac{2\pi}{3} + \phi_p\right] \\ v_{pc,2} = v_p \cos\left[(\omega_p - 2\omega_1)t - \dfrac{2\pi}{3} + \phi_p\right]. \end{cases} \tag{42}$$

After applying the two perturbations, the ac-side impedance matrix is calculated based on the method described in [34] as

$$\mathbf{Z}_{\text{ac}} = -\begin{bmatrix} E_1(j\omega_p) & E_2(j\omega_p) \\ E_1(j\omega_p - j2\omega_1) & E_2(j\omega_p - j2\omega_1) \end{bmatrix} \times \begin{bmatrix} I_{s,1}(j\omega_p) & I_{s,2}(j\omega_p) \\ I_{s,1}(j\omega_p - j2\omega_1) & I_{s,2}(j\omega_p - j2\omega_1) \end{bmatrix}^{-1}, \tag{43}$$

where subscripts 1 and 2 indicate the respective perturbation sets. Since the considered system is linear time-invariant, the resulting impedance is not affected by the initial phase angle of the perturbations. Thus, ϕ_p can be assumed to be equal to zero [15].

1) AC-SIDE IMPEDANCE WITH CLOSED-LOOP VOLTAGE CONTROL

A closed-loop voltage control scheme can be adopted for MMCs that computes the ideal insertion indices based on measured sum-capacitor voltages, i.e.,

$$n_u = \frac{v_c^\star - v_s^\star}{v_{Cu}^\Sigma} \quad \text{and} \quad n_l = \frac{v_c^\star + v_s^\star}{v_{Cl}^\Sigma}. \tag{44}$$

However, this approach yields an asymptotically unstable system which requires additional sum/imbalance arm energy (or alternatively voltage) control to achieve asymptotic stability [31]. Assuming that perfect arm-balancing control is achieved, the response of $v_c^\star$ to the applied perturbation is infinitesimal and/or can be ignored. Thus, the closed-loop output impedance becomes independent of the internal dynamics of the MMC and can be obtained based on the ac-side dynamics, i.e., (5a). The response of the PCC voltage to the applied perturbation is given in (19). Ignoring delays, substituting

$$v_{u,l} = n_{u,l} v_{Cu,l}^\Sigma \tag{45}$$

in (44) yields $v_s = v_s^\star$. Using equations (16), (21)–(29), (31), and (33a) (which are all equations *not* involving internal dynamics of the MMC), the response of $E(j\omega_p)$ and $I_s(j\omega_p)$ to the applied perturbation can be derived analytically by evaluating (5a) and thus, the closed-loop output impedance can be obtained. With compensated modulation, mirror frequency effect is negligible and the output impedance is single-input single-output (SISO), i.e., $|E(j\omega_p - j2\omega_1)| \ll |E(j\omega_p)|$ and $|I_s(j\omega_p - j2\omega_1)| \ll |I_s(j\omega_p)|$. Hence, the closed-loop output impedance can be obtained by

$$Z_{\text{ac}}(j\omega_p) = -\frac{E(j\omega_p)}{I_s(j\omega_p)}. \tag{46}$$

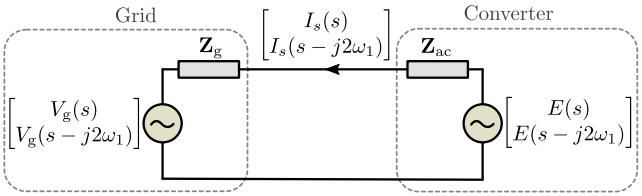

FIGURE 3. Small-signal frequency-domain representation of the grid-connected converter by its Thévenin equivalent circuit.

D. STABILITY ANALYSIS: THE IMPEDANCE-BASED CRITERION

Fig. 3 shows the small-signal representation of the system consisting of the grid-forming converter which is modeled by a voltage source in series with an impedance and a grid represented by a voltage source behind the grid impedance. Grid-forming converters are prone to instability and control interactions in strong grid conditions or when the voltage control bandwidth is low [6]. In this work, the interactions arising from low bandwidth of the voltage control loop are investigated.

The frequency response of the converter current can be obtained as

$$\mathbf{I_s} = \frac{\mathbf{E} - \mathbf{V_g}}{\mathbf{Z_{ac}} + \mathbf{Z_g}}. \tag{47}$$

In order to assess the small-signal stability of the system, two prerequisite conditions apply, namely that,

- E must be stable, i.e., the grid-forming converter must be stable when unloaded;
- Z_g must be stable, i.e., the grid current must be stable when supplied by an ideal voltage-source.

The characteristic equation of the system in (47) is a MIMO system. The right-half-plane zeros of the characteristic equation, i.e., $\mathbf{Z}_{\text{ac}} + \mathbf{Z}_{\mathbf{g}}$ can indicate unstable closed-loop poles. It should be noted that no cross-couplings exist in the grid impedance as it has been modeled in the phase-domain, not the synchronous reference frame. Thus, the determinant of the characteristic equation can be obtained as

$$\det\left[\mathbf{Z}_{\text{ac}} + \mathbf{Z}_{\mathbf{g}}\right] = (Z_{11} + Z_{g,11})(Z_{22} + Z_{g,22}) - Z_{12}Z_{21}\,, \tag{48}$$

where

$$Z_{g,11} = R_g + j\omega_p L_g \tag{49a}$$

$$Z_{g,22} = R_g + j\left[(\omega_p - j2\omega_1)L_g\right]. \tag{49b}$$

After mathematical manipulations, the determinant can be reformulated as

$$1 + \frac{Z_{11} - \frac{Z_{12}Z_{21}}{Z_{22}+Z_{g,22}}}{Z_{g,11}} = 1 + \frac{Z_{\text{eq,ac}}}{Z_{g,11}}\,, \tag{50}$$

where $Z_{\text{eq,ac}}$ is the equivalent single-input single-output ac-side impedance of the MMC taking into account its interaction with the grid impedance [21]. If the two prerequisites defined above are satisfied, the minor-loop gain defined as $Z_{\text{eq,ac}}/Z_{g,11}$ can be used to assess the small-signal stability of the system via the Nyquist stability criterion.

IV. RESULTS AND DISCUSSIONS

The impedance obtained via the analytical model developed above is validated against that obtained from post-processing the PCC voltage and current waveforms in simulations and in a down-scaled experimental setup. The analytical impedance model is then used to analyze and showcase the system stability. A logarithmically spaced set of perturbation frequencies between 1 Hz and 200 Hz is considered.

Fig. 4 shows the ac-side impedances of an MMC with direct voltage control, with closed-loop voltage control, and for comparison that of a two-level converter. For the two level converter, a phase inductance equal to half the arm inductances of the equivalent MMC is opted. It can be seen that with closed-loop voltage control, the ac-side impedance of the MMC is similar to that of the two-level converter, implying that they exhibit the same behavior on the ac-side. The closed-loop output impedance of the MMC with direct voltage control, however, is different due to the influence of the internal dynamics of the MMC on the impedance. A non-passive frequency region ($\phi_{\text{Zac}} < -90°$) exists around the fundamental frequency in all cases which is a byproduct of the applied grid-forming control shown in Fig. 2. For the ease of hardware implementation, the direct voltage control scheme is assumed in the remainder of the study to demonstrate the workings of the proposed active damping methods.

A. SIMULATION RESULTS

A simulation model of an MMC-based HVDC system is built in MATLAB/Simulink. The ac-side of an MMC-based HVDC system is considered, neglecting the dc-side dynamics, i.e., a stiff voltage source on the dc-bus is assumed. The parameters of the simulated system are summarized in Tables 1 and 2. Fig. 5 shows the Bode diagram of the ac-side impedance of the HVDC converter $\mathbf{Z}_{\text{ac}}$, indicating a close match between the analytical impedance model and the impedance measured via simulations. Fig. 6 shows the equivalent single-input single-output closed-loop output (ac-side) impedance of the HVDC converter when the integral gain of the voltage controller is reduced, and the grid impedance. With a low integral gain, a narrower band with negative resistance ($\phi_{\text{Zac,eq}} < -90°$) exists below the fundamental frequency and at the magnitude intersection point of 46.7 Hz, the phase margin of the minor-loop gain is negative. Fig. 7 shows the Nyquist diagram of the minor-loop

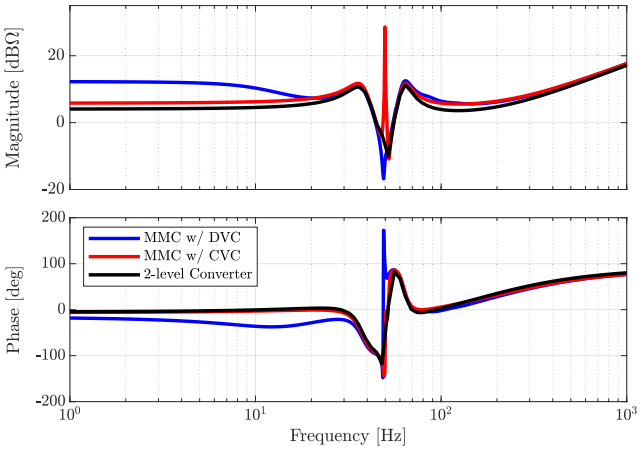

FIGURE 4. Bode diagram of the ac-side impedance $Z_{\text{eq,ac}}$ of an MMC with direct voltage control (blue), an MMC with closed-loop voltage control (red), and a two-level converter (black).

TABLE 1. Simulation system parameters.

Dc-bus voltage	v_{dc}	800	kV
Ac grid voltage amplitude	v_g	320	kV
Converter rated power	S_c	1000	MVA
Fundamental frequency	f_1	50	Hz
Arm inductance	L	60	mH
Arm resistance	R	0.2	Ω
Submodule capacitance	C_{SM}	7	mF
Number of submodules per arm	N	200	
Short-circuit ratio	k_{sc}	4.5	
Grid impedance ratio	k_{XR}	30	

TABLE 2. Controller settings of the simulation model of the HVDC system.

Active power reference	$P^\star$	800	MW
Reactive power reference	$Q^\star$	0	VAr
Voltage controller proportional gain	$k_{p,v}$	0.0002	A/V
Voltage controller integral gain	$k_{i,v}$	2	A/(Vs)
Ac-side current control system bandwidth	α_s	1200	rad/s
Ac-side current integral control gain	α_1	100	rad/s
Circulating current control system bandwidth	α_c	1000	rad/s
Circulating current integral control gain	α_2	100	rad/s
Active power droop gain	m_P	6.3×10^{-9}	
Reactive power droop gain	n_Q	6.4×10^{-5}	

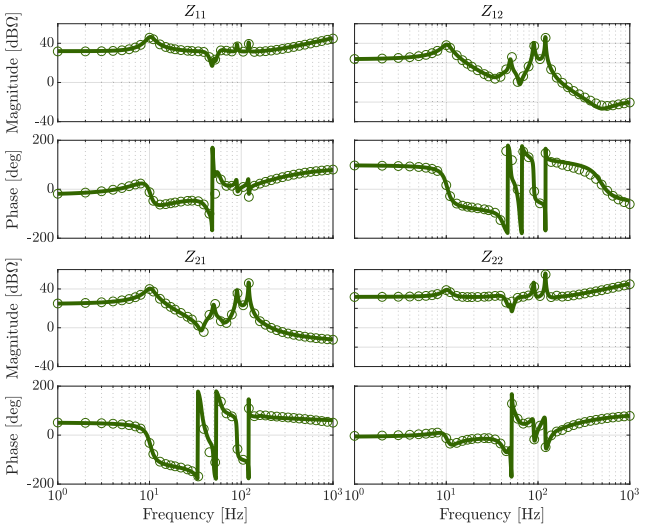

FIGURE 5. Bode diagram of the ac-side impedance of a droop-controlled grid-forming MMC-HVDC with dual-loop voltage control. The solid lines show the analytical impedance, and the circles demonstrate the measured impedance in simulations.

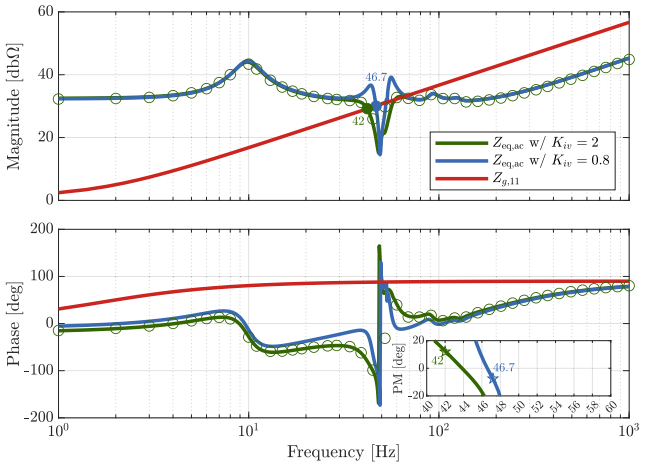

FIGURE 6. Bode diagram of the equivalent ac-side impedance of the converter $Z_{eq,ac}$ for different values of the integral gain of the voltage controller and the grid impedance $Z_{g,11}$. The asterisks indicate simulation results. The close-up box shows the phase margin of $Z_{eq,ac}/Z_{g,11}$ for the two cases.

gain of the system for the two cases studied in Fig. 6. It can be observed that with a low integral gain, the contour encircles the $(-1, 0)$ critical point, implying the instability of the system.

B. THE EXPERIMENTAL SETUP

Fig. 8 shows the experimental setup used in this work. An MMC with one half-bridge submodule per arm (based on SiC MOSFETs) is assembled. The control system is implemented on a rapid control prototyping platform by Imperix which utilizes fully programmable digital signal processing (DSP) and field-programmable gate array (FPGA) units. External current and voltage sensors placed on the back plane of the rack measure the arm currents and the PCC

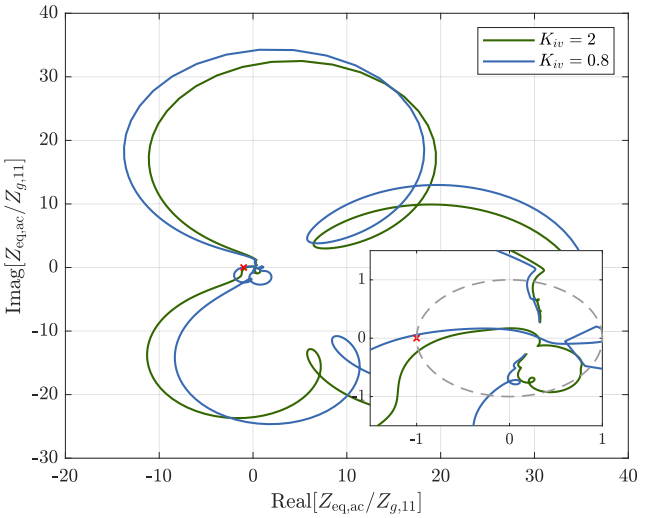

FIGURE 7. Nyquist diagram of $Z_{eq,ac}/Z_{g,11}$ for droop-controlled grid-forming MMC with dual-loop voltage control in the simulation model of the HVDC system.

TABLE 3. Experimental setup parameters.

Ac grid voltage amplitude	v_g	48	V
Dc-bus voltage	v_{dc}	130	V
Fundamental frequency	f_1	50	Hz
Arm inductance	L	2.5	mH
Arm resistance	R	0.65	Ω
Grid inductance	L_g	5	mH
Grid resistance	R_g	0.1	Ω
Submodule capacitance	C_{SM}	1	mF
Perturbation frequency	f_p	1–200	Hz
Perturbation amplitude	v_p	2.5	V
Number of submodules per arm	N	1	

TABLE 4. Controller settings of the experimental setup.

Active power reference	$P^\star$	300	W
Reactive power reference	$Q^\star$	0	VAr
Voltage controller proportional gain	$k_{p,v}$	0.002	A/V
Voltage controller integral gain	$k_{i,v}$	40	A/(Vs)
Ac-side current control system bandwidth	α_s	1200	rad/s
Ac-side current integral control gain	α_1	100	rad/s
Circulating current control system bandwidth	α_c	1000	rad/s
Circulating current integral control gain	α_2	100	rad/s
Active power droop gain	m_P	0.0063	
Reactive power droop gain	n_Q	0.0096	
carrier frequency ratio	f_c/f_1	402.66	

voltages that are used to control the system quantities, see Fig. 2. A phase-shifted pulse-width modulation (PSC-PWM) scheme has been used that ensures individual capacitor voltage balancing provided that the carrier frequency is a non-integer multiple of the fundamental frequency [35]. The system and control parameters of the experimental setup are given in Tables 3 and 4, respectively.

A Chroma regenerative grid simulator is used as the three-phase ac grid and also as the perturbation source. The perturbation signals are superimposed on the grid

FIGURE 8. The experimental setup.

voltage by overlaying desired perturbation frequencies on the reference voltage of the grid simulator. An inductive-resistive impedance models the grid weakness.

The ac-side impedance is measured by perturbing the grid voltage with two independent perturbation sets through externally amplifying the voltage of the regenerative grid simulator. The measured voltages and currents are then post-processed to obtain the measured ac-side impedance matrix of the converter.

C. IMPACT OF CONTROL ON CLOSED-LOOP OUTPUT IMPEDANCE

The choice of control solutions and selected control gains can impact the equivalent ac-side impedance. A single-loop voltage control is the simplest form that the control of the PCC voltage can be realized in grid-forming applications [23]. In this control scheme, there is no explicit control of ac-side currents. The ac-side impedance of the MMC with single-loop voltage control is shown in Fig. 9. As seen in the figure, non-passive frequency regions exist around the fundamental frequency in Z_{11}. It is also evident from the magnitude plots that the impact of the direct term impedances are more pronounced than the cross-coupling terms, indicating that the equivalent impedance is impacted more by Z_{11} and Z_{22}, rather than the cross-coupling impedances.

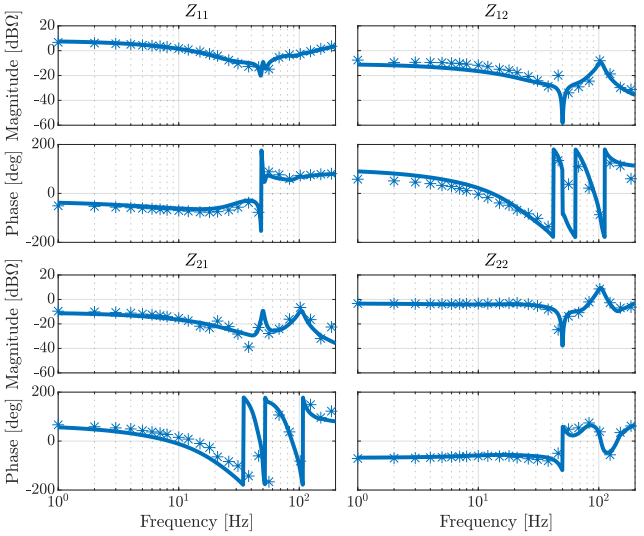

FIGURE 9. Bode diagram of the ac-side impedance of a droop-controlled grid-forming MMC with single-loop voltage control. The solid lines show the analytical impedance, and the asterisks demonstrate the measured impedance from the experimental prototype.

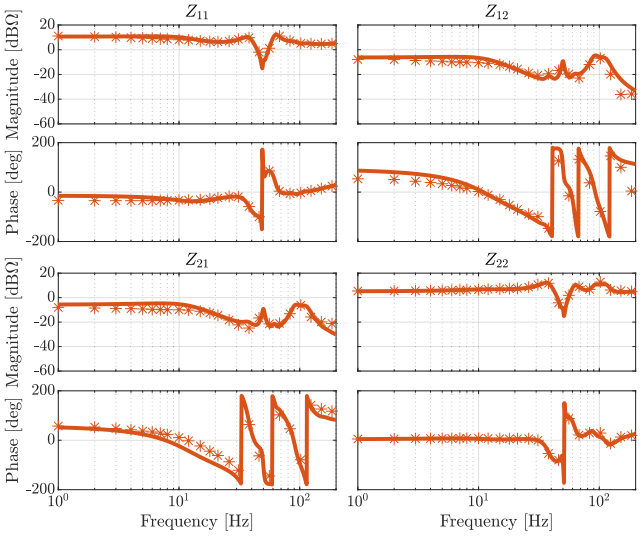

FIGURE 10. Bode diagram of the ac-side impedance of a droop-controlled grid-forming MMC with dual-loop voltage control. The solid lines show the analytical impedance, and the asterisks demonstrate the measured impedance from the experimental prototype.

Fig. 10 shows the ac-side impedance of the MMC with dual-loop voltage control, i.e., the default form in this work as shown in Fig. 2. Differences exist between the impedance with dual-loop versus the single-loop case, especially around the fundamental frequency where the impedance of the dual-loop control case has a more pronounced valley in magnitude of Z_{11} and non-passive behavior in Z_{22}. In addition, the impedance magnitudes are greater in value with dual-loop control at frequencies other than the fundamental frequency.

Fig. 11 shows the equivalent ac-side impedance of the converter $Z_{\text{eq,ac}}$ and the grid impedance $Z_{g,11}$, when the integral gain of the voltage controller is altered. When

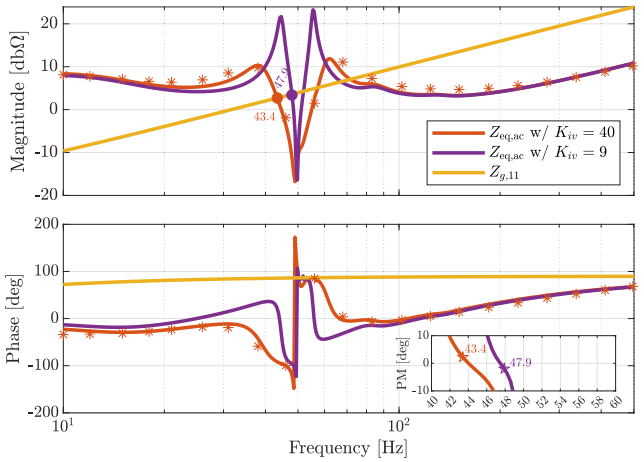

FIGURE 11. Bode diagram of the equivalent ac-side impedance of the converter $Z_{eq,ac}$ for different values of the integral gain of the voltage controller and the grid impedance $Z_{g,11}$. The asterisks indicate experimental results. The close-up box shows the phase margin of $Z_{eq,ac}/Z_{g,11}$ for the two cases.

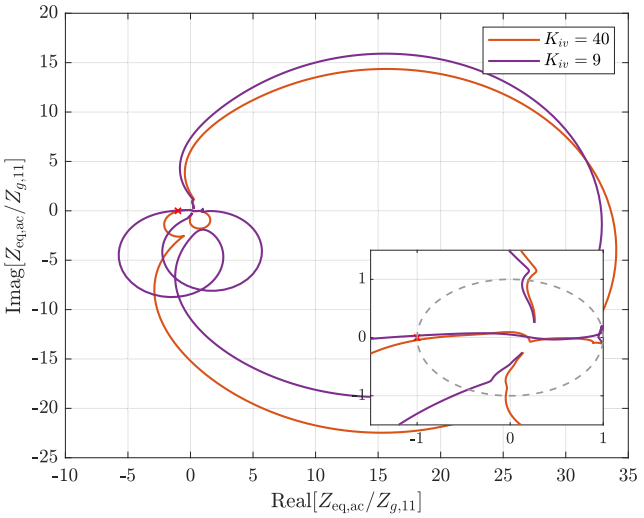

FIGURE 12. Nyquist diagram of $Z_{eq,ac}/Z_{g,11}$ for droop-controlled grid-forming MMC with dual-loop voltage control for the experimental setup. The contour encircles $(-1, 0)$ with low integral gain indicating an unstable system. A close-up visualizing the critical point is also shown.

the integral gain is high, the resonance at the fundamental frequency has a wide bandwidth as observed in the impedance magnitude plot. In this case, there are intersection points between the converter equivalent impedance and the grid impedance at 43.4 Hz, 57.4 Hz and 71.8 Hz. At all of these points, the phase margin is positive, indicating that the system is stable. When k_{iv} is reduced, the bandwidth of the resonance at the fundamental frequency gets narrower, and the intersection points move to 47.9, 51.9 and 67.4 Hz, respectively. The phase margin of the two systems with different integral gains of the voltage controller are shown in the zoomed-in phase plot of the same figure. As highlighted in the figure, at $f = 47.9$ Hz, the phase margin of the minor-loop gain of the case with a low integral gain of the controller is below zero. This indicates a risk of small-signal instability. Nevertheless, the stability has to be verified with the Nyquist stability criterion which is a necessary and sufficient condition for stability.

The Nyquist diagram of the single-input single-output minor loop gain of the system, i.e., $Z_{eq,ac}/Z_{g,11}$, shown in Fig. 12 indicates that the system does go unstable when the integral gain of the voltage controller is decreased. As expected, the contours intersect with the unit circle three times corresponding to the three intersections in the Bode diagram of the impedance magnitudes. Unstable oscillations in the phase variables, therefore, should occur at the predicted frequency of $f_{osc} = 47.9$ Hz. Due to Park transformation, the frequency of the oscillations in direct (*non-alternating*) system variables is at $f_{osc,dq} = 50 - 47.9 = 2.1$ Hz.

D. ACTIVE DAMPING TECHNIQUES

Filter-based active damping to handle stability issues in grid-following systems has been established in [36] and [37]. Three active damping methods for grid-forming converters are presented in this work that can add phase lead to the system around the fundamental frequency in order to stabilize the system. In this way they indirectly modify also the ac-side impedance at these frequencies. Fig. 13 summarizes the presented modifications that improve the phase margin and therefore, the small-signal stability.

A virtual resistance on the path of the ac-side currents damps the ac-side impedance around the fundamental frequency. Virtual resistances R_v can be added in a cross-coupling fashion to the input reference of the current controller similar to that presented in [26]. The value of the R_v gain can be selected based on trial and error. To this end, the Nyquist diagram of the minor loop-gain of the closed-loop system can be drawn and a suitable value that ensures closed-loop stability and suitable phase margin can be selected. In the case studies of this work, a gain of $R_v = 0.2$ for simulations and $R_v = 0.9$ in the experimental setup is chosen. In the impedance model, the responses of the ac-side voltage references in the dq-frame to the applied perturbation are modified as

$$V^{\star}_{s,dq}(j\omega) = F_{s,dq}(j\omega)[I^{\star}_{s,dq}(j\omega) - I_{s,dq}(j\omega) \pm R_v I_{s,qd}(j\omega)] \mp \frac{\omega_1 L}{2} I_{s,qd}(j\omega)\,, \tag{51}$$

where $\omega = \omega_p - \omega_1$.

Alternatively, the dq-frame currents can be filtered at a lower frequency than the predicted oscillation. A first-order low-pass filter of the form

$$G_{\mathrm{LPF}}(s) = \frac{\omega_{\mathrm{lpf}}}{s + \omega_{\mathrm{lpf}}}\,, \tag{52}$$

is used in this work with a cut-off frequency of $2\pi 3$ rad/s in the HVDC system simulation and $2\pi 1.5$ rad/s in the experimental setup. The cut-off frequencies are chosen to be lower than the predicted oscillation frequencies which

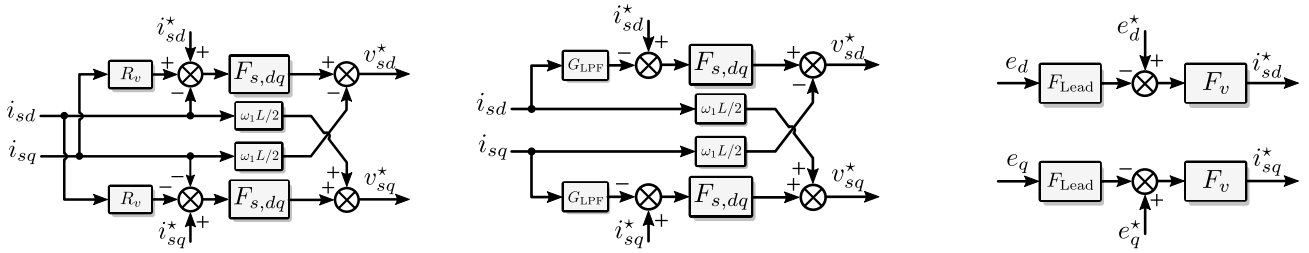

(a) cross-coupled virtual resistance. (b) ac-current low-pass filter. (c) PCC voltage lead compensator.

FIGURE 13. Proposed active damping techniques to increase system phase margin.

are 3.3 Hz for the simulation case study, and 2.1 Hz in the experimental work. In this way, extra damping is provided by diminishing the oscillations that enter the current control loop. In the frequency-domain, the harmonic responses of the ac-side voltage references are modified to

$$V^\star_{s,dq}(j\omega) = F_{s,dq}(j\omega)[I^\star_{s,dq}(j\omega) - G_{\text{LPF}}(j\omega)I_{s,dq}(j\omega)] \mp \frac{\omega_1 L}{2} I_{s,qd}(j\omega)\,, \tag{53}$$

where $\omega = \omega_p - \omega_1$.

A third option is to cascade a lead compensator on the path of the synchronous reference frame PCC voltage measurements. Lead compensators add phase to the control loop, affecting the converter impedance and improving the stability. In this work, a first-order lead compensator of the form

$$F_{\text{Lead}}(s) = \frac{1 + T_1 s}{1 + T_2 s}\,, \tag{54}$$

has been designed that adds phase around 2 Hz to the PCC voltages in the *dq*-frame, and indirectly improves the impedance phase. To this end, the time constants of the compensator are selected as $T_1 = 0.1$ and $T_2 = 0.05$. Fig. 14 shows the Bode diagram of the designed lead compensator in this case. The selected compensator is shown to be able to sufficiently dampen the predicted oscillation both in the simulation case study and in the experimental work. Adding phase lead to the measured ac-side voltages translates in the frequency domain to modifying the ac-side current references to

$$I^\star_{s,dq}(j\omega) = F_v(j\omega)\big(E^\star_{dq}(\omega) - F_{\text{Lead}}(j\omega)E_{dq}(\omega)\big)\,, \tag{55}$$

where $\omega = \omega_p - \omega_1$. The tuning of appropriate compensator poles and zeros can be done by quantifying the phase and gain margins off the Nyquist diagram of the minor loop-gain that is obtained by using the developed ac-side impedance model.

Using each one of the three proposed active damping methods provides enough phase lead at non-passive frequencies around the fundamental frequency such that the system stabilizes with a positive phase margin. Fig. 15 shows the simulation results of the HVDC system. It is observed that in $t < 2$ s and $t > 8$ s with a low integral gain the system is unstable. When the active damping loops are enabled, the system stabilizes, albeit with different dynamic responses.

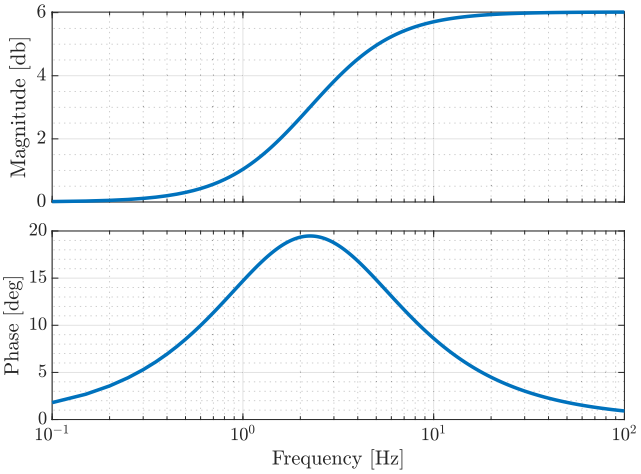

FIGURE 14. Bode diagram of the lead compensator $F_{\text{Lead}}(s)$.

The transient behavior is largely dependent on the design of the filters and the choice of the gains.

Fig. 16 shows the waveforms of the converter variables during experiments with a laboratory setup to verify the unstable case studies and the performance of the stabilizing active damping techniques. The integral gain of the voltage controller is manipulated to cause system instability. The stabilizing loops are then enabled for a short duration starting at $t = 2$ s and disabled at $t = 8$ s. As seen in the figure, unstable oscillations are present in the system before $t = 2$ s when the stabilizing loops are bypassed. The frequency of the oscillations is computed using a fast Fourier transform of the signals during the instability, and corresponds to the predicted $f_{\text{osc},dq} = 2.1$ Hz for the variables in the direct reference frame, as seen in Fig. 17. The system is stabilized upon enabling of the damping compensators in all cases. As an example, Fig. 18 shows the harmonic responses of the ac-side current and the PCC voltage to the applied perturbation with and without the virtual resistance loop for the experimental case study. As seen in the figure, as a result of the virtual resistance loop, the predicted oscillations at 47.9 Hz in the system are dampened and no longer appear.

Fig. 19 shows the Nyquist diagram of the minor loop gain $Z_{\text{eq,ac}}/Z_{g,11}$ with and without the active damping compensators, for the simulations of the HVDC system and the

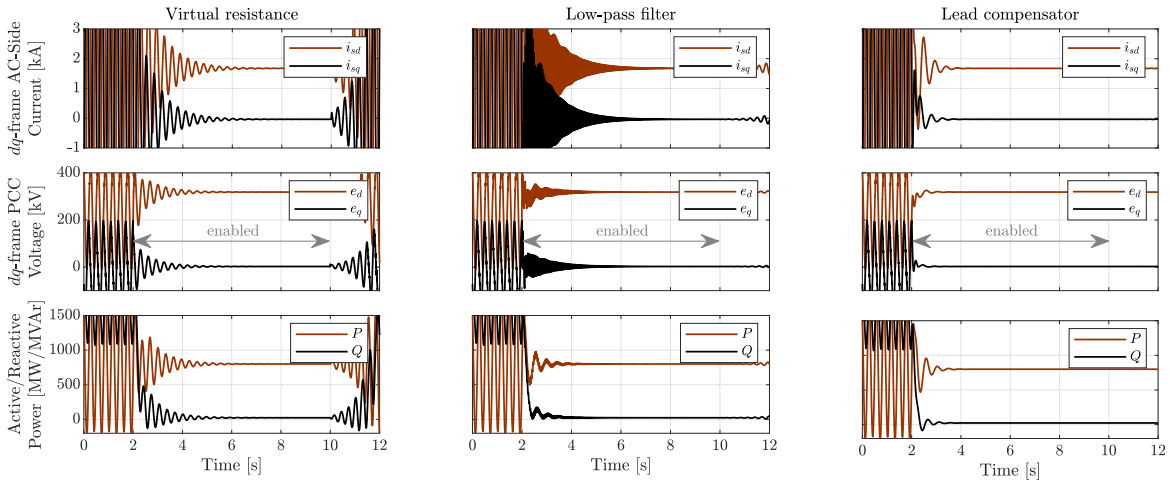

FIGURE 15. Time-domain verification of the instability scenarios and the impact of proposed modifications in simulations of the HVDC system. The stabilizing loops are enabled at $t = 2$ s and disabled at $t = 10$ s.

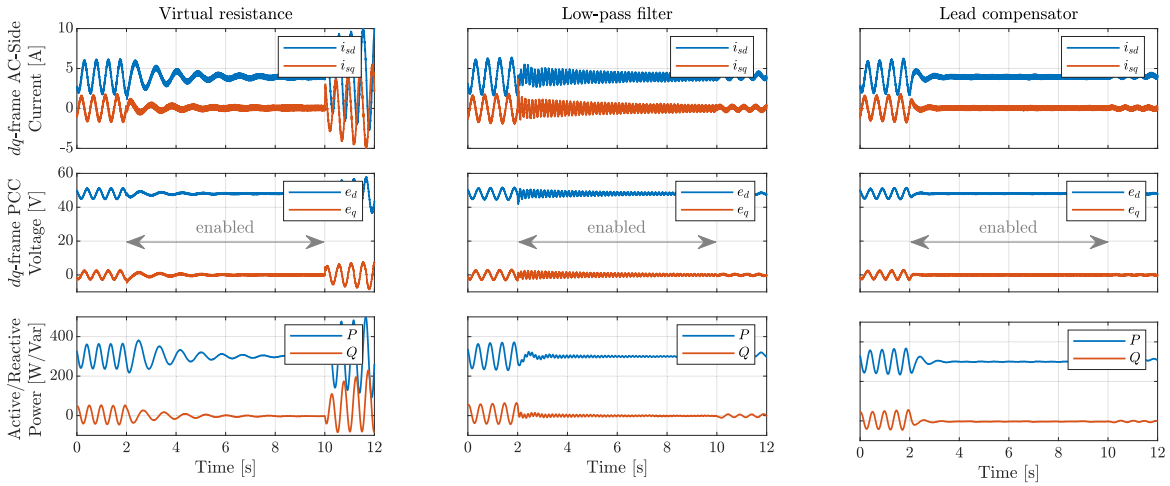

FIGURE 16. Experimental time-domain verification of the instability scenarios and the impact of proposed modifications. The stabilizing loops are enabled at $t = 2$ s and disabled at $t = 10$ s.

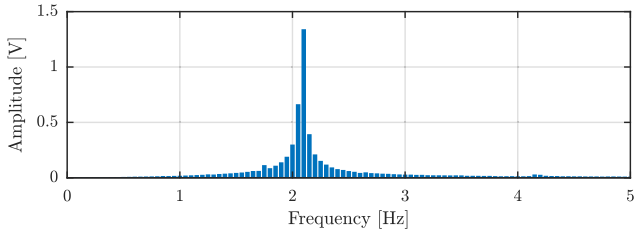

FIGURE 17. Fast Fourier transform of e_q during instability based on recording from the experiments.

down-scaled laboratory prototype. It can be concluded from the time-domain results and frequency-domain verification that the proposed loops successfully stabilize the system as the contours no longer encircle the $(-1, 0)$ point. Future research on the topic is required to unravel the small-signal stability conditions for grid-forming converters connected in

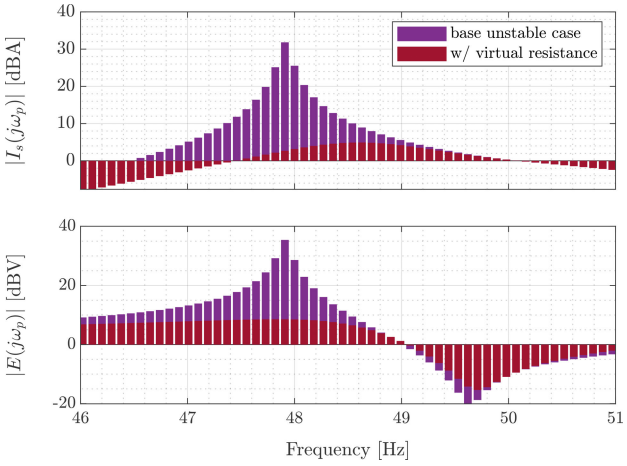

FIGURE 18. Fourier coefficient magnitudes of i_s (top) and e (bottom) to the applied perturbation with and without the cross-coupled virtual resistance loop.

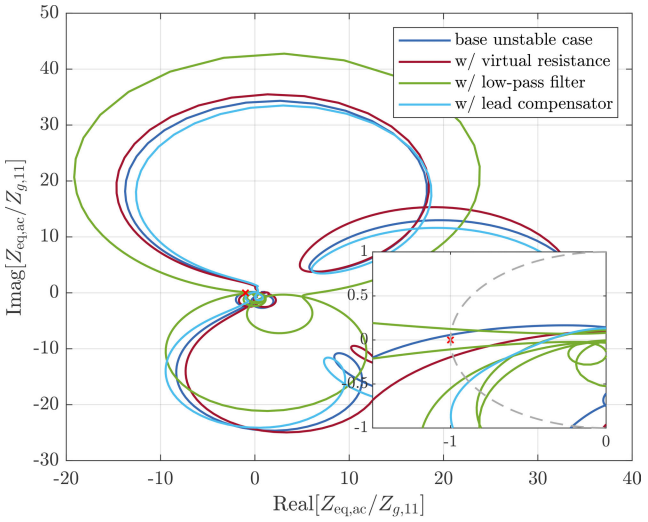

(a) simulations (HVDC system).

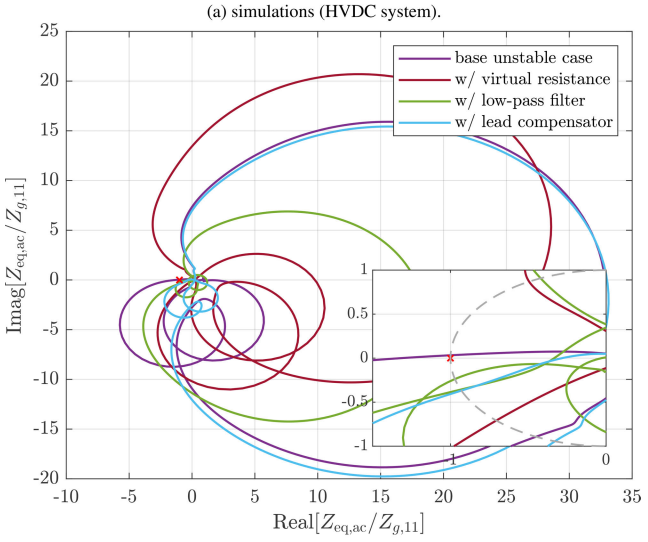

(b) down-scaled laboratory prototype.

FIGURE 19. Nyquist diagram of $Z_{eq,ac}/Z_{g,11}$. The base unstable case's contour encircles $(-1, 0)$ indicating an unstable system. For all other cases the Nyquist diagram predicts a stable system.

parallel both in grid-connected and off-grid conditions, the effect of modulation schemes on the ac-side impedance of the MMCs in grid-forming control mode, and the impact of discretization of the control system on the terminal impedance and the system stability.

V. CONCLUSION

This paper presents an analytical ac-side impedance model of a droop-controlled grid-forming modular multilevel converter. The effect of single-loop and dual-loop voltage grid-forming control schemes on the closed-loop output impedance of the converter is analyzed, followed by showcasing a possible subsynchronous control interactions of the converter with the grid. It is shown that the parameters of the voltage controller can impact the small-signal stability of the grid-connected converter. Three stabilizing loops based on 1) virtual resistance added to ac-side currents, 2) low-pass filters in the path of ac-side currents, and 3) lead compensators in the path of PCC voltage have been proposed in order to omit the small-signal instability and improve stability margins. Experimental results verified on a down-scaled laboratory prototype validate the accuracy of the developed analytical model and the workings of the proposed stabilizing compensators. It is shown that the unstable oscillations and their frequencies can be accurately predicted, and the proposed active damping techniques can bring the system back to stability.

REFERENCES

[1] A. Yazdani and R. Iravani, *Voltage-Sourced Converters in Power Systems: Modeling, Control, and Applications*. Hoboken, NJ, USA: Wiley, 2010.

[2] N. Flourentzou, V. G. Agelidis, and G. D. Demetriades, "VSC-based HVDC power transmission systems: An overview," *IEEE Trans. Power Electron.*, vol. 24, no. 3, pp. 592–602, Mar. 2009.

[3] A. Lesnicar and R. Marquardt, "An innovative modular multilevel converter topology suitable for a wide power range," in *Proc. IEEE Bologna Power Tech Conf.*, vol. 3, Bologna, Italy, Jun. 2003, pp. 1–6.

[4] X. Wang and F. Blaabjerg, "Harmonic stability in power electronic-based power systems: Concept, modeling, and analysis," *IEEE Trans. Smart Grid*, vol. 10, no. 3, pp. 2858–2870, May 2019.

[5] S. D'Arco and J. A. Suul, "Equivalence of virtual synchronous machines and frequency-droops for converter-based microgrids," *IEEE Trans. Smart Grid*, vol. 5, no. 1, pp. 394–395, Jan. 2014.

[6] Y. Li, Y. Gu, and T. C. Green, "Revisiting grid-forming and grid-following inverters: A duality theory," *IEEE Trans. Power Syst.*, vol. 37, no. 6, pp. 4541–4554, Nov. 2022.

[7] C. Buchhagen, C. Rauscher, A. Menze, and J. Jung, "BorWin1—First experiences with harmonic interactions in converter dominated grids," in *Proc. Int. ETG Congr., Die Energiewende Blueprints New Energy Age*, Nov. 2015, pp. 1–7.

[8] H. Saad, Y. Fillion, S. Deschanvres, Y. Vernay, and S. Dennetière, "On resonances and harmonics in HVDC-MMC station connected to AC grid," *IEEE Trans. Power Del.*, vol. 32, no. 3, pp. 1565–1573, Jun. 2017.

[9] L. Harnefors, A. G. Yepes, A. Vidal, and J. Doval-Gandoy, "Passivity-based controller design of grid-connected VSCs for prevention of electrical resonance instability," *IEEE Trans. Ind. Electron.*, vol. 62, no. 2, pp. 702–710, Feb. 2015.

[10] M. Amin and M. Molinas, "Understanding the origin of oscillatory phenomena observed between wind farms and HVdc systems," *IEEE J. Emerg. Sel. Topics Power Electron.*, vol. 5, no. 1, pp. 378–392, Mar. 2017.

[11] J. Sun, "Impedance-based stability criterion for grid-connected inverters," *IEEE Trans. Power Electron.*, vol. 26, no. 11, pp. 3075–3078, Nov. 2011.

[12] M. Beza, M. Bongiorno, and G. Stamatiou, "Analytical derivation of the AC-side input admittance of a modular multilevel converter with open- and closed-loop control strategies," *IEEE Trans. Power Del.*, vol. 33, no. 1, pp. 248–256, Feb. 2018.

[13] J. Khazaei, M. Beza, and M. Bongiorno, "Impedance analysis of modular multi-level converters connected to weak AC grids," *IEEE Trans. Power Syst.*, vol. 33, no. 4, pp. 4015–4025, Jul. 2018.

[14] G. Stamatiou, M. Beza, M. Bongiorno, and L. Harnefors, "Analytical derivation of the DC-side input admittance of the direct-voltage controlled modular multilevel converter," *IET Gener., Transmiss. Distrib.*, vol. 11, no. 16, pp. 4018–4030, Nov. 2017.

[15] J. Sun and H. Liu, "Sequence impedance modeling of modular multilevel converters," *IEEE J. Emerg. Sel. Topics Power Electron.*, vol. 5, no. 4, pp. 1427–1443, Dec. 2017.

[16] Z. Li, Z. Wang, Y. Wang, T. Yin, N. Mei, B. Yue, and W. Lei, "Accurate impedance modeling and control strategy for improving the stability of DC system in multiterminal MMC-based DC grid," *IEEE Trans. Power Electron.*, vol. 35, no. 10, pp. 10026–10049, Oct. 2020.

[17] Z. Xu, B. Li, L. Han, J. Hu, S. Wang, S. Zhang, and D. Xu, "A complete HSS-based impedance model of MMC considering grid impedance coupling," *IEEE Trans. Power Electron.*, vol. 35, no. 12, pp. 12929–12948, Dec. 2020.

[18] L. Bessegato, K. Ilves, L. Harnefors, and S. Norrga, "Effects of control on the AC-side admittance of a modular multilevel converter," *IEEE Trans. Power Electron.*, vol. 34, no. 8, pp. 7206–7220, Aug. 2019.
[19] M. Nahalparvari, M. Asoodar, L. Bessegato, S. Norrga, and H.-P. Nee, "Modeling and shaping of the DC-side admittance of a modular multilevel converter under closed-loop voltage control," *IEEE Trans. Power Electron.*, vol. 36, no. 6, pp. 7294–7306, Jun. 2021.
[20] H. Wu, X. Wang, L. Kocewiak, and L. Harnefors, "AC impedance modeling of modular multilevel converters and two-level voltage-source converters: Similarities and differences," in *Proc. IEEE 19th Workshop Control Model. Power Electron. (COMPEL)*, Jun. 2018, pp. 1–8.
[21] Y. Liao, X. Wang, F. Liu, K. Xin, and Y. Liu, "Sub-synchronous control interaction in grid-forming VSCs with droop control," in *Proc. 4th IEEE Workshop Electron. Grid (eGRID)*, Nov. 2019, pp. 1–6.
[22] Y. Liao and X. Wang, "Controller design-oriented analysis of grid-forming converters for stability robustness enhancement," *Chin. J. Electr. Eng.*, vol. 7, no. 4, pp. 37–48, Dec. 2021.
[23] Y. Liao, X. Wang, and F. Blaabjerg, "Passivity-based analysis and design of linear voltage controllers for voltage-source converters," *IEEE Open J. Ind. Electron. Soc.*, vol. 1, pp. 114–126, 2020.
[24] C. M. Freitas, E. H. Watanabe, and L. F. C. Monteiro, "Grid-forming MMC: A comparison between single- and dual-loop control approaches," in *Proc. Brazilian Power Electron. Conf. (COBEP)*, Nov. 2021, pp. 1–6.
[25] J. Lyu, X. Cai, and M. Molinas, "Frequency domain stability analysis of MMC-based HVdc for wind farm integration," *IEEE J. Emerg. Sel. Topics Power Electron.*, vol. 4, no. 1, pp. 141–151, Mar. 2016.
[26] R. Pan, G. Tang, S. Liu, and Z. He, "Impedance analysis of grid forming control based modular multilevel converters," *J. Modern Power Syst. Clean Energy*, vol. 11, no. 3, pp. 967–979, May 2023.
[27] H. Guo, Z. Zhang, and Z. Xu, "Impedance modelling and stability analysis of modular multilevel converter with different types of grid-forming control schemes," *IET Gener., Transmiss. Distrib.*, vol. 17, no. 2, pp. 337–353, Jan. 2023.
[28] L. Lin, Q. Zeng, J. Zhu, X. Shi, and J. Hu, "High-frequency oscillation mechanism analysis and suppression strategy of grid-forming control MMC-HVDC," *IEEE Trans. Power Del.*, vol. 38, no. 3, pp. 1588–1600, Jun. 2023.
[29] L. Harnefors, A. Antonopoulos, S. Norrga, L. Ängquist, and H.-P. Nee, "Dynamic analysis of modular multilevel converters," *IEEE Trans. Ind. Electron.*, vol. 60, no. 7, pp. 2526–2537, Jul. 2013.
[30] K. Sharifabadi, L. Harnefors, H.-P. Nee, S. Norrga, and R. Teodorescu, *Design, Control, and Application of Modular Multilevel Converters for HVDC Transmission Systems*. Chichester, U.K.: Wiley, 2016.
[31] A. Antonopoulos, L. Angquist, and H.-P. Nee, "On dynamics and voltage control of the modular multilevel converter," in *Proc. 13th Eur. Conf. Power Electron. Appl.*, Sep. 2009, pp. 1–10.
[32] M. Cespedes and J. Sun, "Impedance modeling and analysis of grid-connected voltage-source converters," *IEEE Trans. Power Electron.*, vol. 29, no. 3, pp. 1254–1261, Mar. 2014.
[33] A. Rygg, M. Molinas, C. Zhang, and X. Cai, "A modified sequence-domain impedance definition and its equivalence to the dq-domain impedance definition for the stability analysis of AC power electronic systems," *IEEE J. Emerg. Sel. Topics Power Electron.*, vol. 4, no. 4, pp. 1383–1396, Dec. 2016.
[34] Y. Liao and X. Wang, "Stationary-frame complex-valued frequency-domain modeling of three-phase power converters," *IEEE J. Emerg. Sel. Topics Power Electron.*, vol. 8, no. 2, pp. 1922–1933, Jun. 2020.
[35] K. Ilves, L. Harnefors, S. Norrga, and H.-P. Nee, "Analysis and operation of modular multilevel converters with phase-shifted carrier PWM," *IEEE Trans. Power Electron.*, vol. 30, no. 1, pp. 268–283, Jan. 2015.
[36] J. Dannehl, M. Liserre, and F. W. Fuchs, "Filter-based active damping of voltage source converters with *LCL* filter," *IEEE Trans. Ind. Electron.*, vol. 58, no. 8, pp. 3623–3633, Aug. 2011.
[37] X. Wang, F. Blaabjerg, and P. C. Loh, "Grid-current-feedback active damping for LCL resonance in grid-connected voltage-source converters," *IEEE Trans. Power Electron.*, vol. 31, no. 1, pp. 213–223, Jan. 2016.

MEHRDAD NAHALPARVARI (Graduate Student Member, IEEE) received the M.Sc. degree in power electronics from Tampere University, Tampere, Finland, in 2019. He is currently pursuing the Ph.D. degree in electrical engineering with the KTH Royal Institute of Technology, Stockholm, Sweden. His research interests include modeling and control of power electronic converters.

MOHSEN ASOODAR (Graduate Student Member, IEEE) received the M.Sc. degree in electrical engineering from the KTH Royal Institute of Technology, Stockholm, Sweden, in 2014. In 2014, he joined ABB's Corporate Research Center, Västerås, Sweden, as a Research Scientist, and later served as a Research and Development Engineer at ABB FACTS, Västerås. He is currently working with Hitachi Energy, Sweden, as a Senior Research and Development Engineer and conducting his industrial PhD studies in collaboration with the KTH Royal Institute of Technology. His research interests include design, control, and grid integration of power electronic systems.

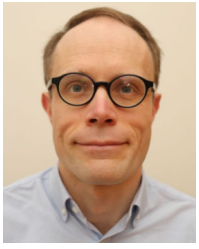

STAFFAN NORRGA (Member, IEEE) was born in Lidingö, Sweden, in 1968. He received the M.Sc. degree in applied physics from the Linköping Institute of Technology, Linköping, Sweden, in 1993, and the Ph.D. degree in electrical engineering from the KTH Royal Institute of Technology, Stockholm, Sweden, in 2005. From 1994 to 2011, he was a Development Engineer with ABB, Västerås, Sweden, in various power-electronics-related areas, such as railway traction systems and converters for HVdc power transmission systems. He is currently an Associate Professor in power electronics with the KTH Royal Institute of Technology. He is the inventor or co-inventor of more than ten granted patents. He has authored or coauthored more than 100 scientific papers published at international conferences or in journals. His research interests include power electronics and its applications in power grids, renewables, and electric vehicles.

HANS-PETER NEE (Fellow, IEEE) was born in Västerås, Sweden, in 1963. He received the M.Sc., Licentiate, and Ph.D. degrees in electrical engineering from the KTH Royal Institute of Technology, Stockholm, Sweden, in 1987, 1992, and 1996, respectively. Since 1999, he has been a Professor of power electronics with the Department of Electrical Engineering, KTH Royal Institute of Technology. His research interests include power electronic converters, semiconductor components, and control aspects of utility applications, such as flexible ac transmission systems, high-voltage direct-current transmission, and variable-speed drives. He was a member of the Board of the IEEE Sweden Section for many years, and also the Chair of the Board, from 2002 to 2003. He is a member of the European Power Electronics and Drives Association and is involved with its Executive Council and International Scientific Committee.